

Analysis and measurement of vibration characteristics of a hollowing defect based on a laser self-mixing interferometer

Yu-Xin Chen(陈煜昕), Jin-Bo Chen(陈金波), Peng Cao(曹鹏), You-Guang Zhao(赵有光), Jun Wang(王钧), Xu-Wei Teng(滕旭玮), and Chi Wang(王驰)

Citation: Chin. Phys. B, 2024, 33 (**12**): 124301. DOI: 10.1088/1674-1056/ad7e99
Journal homepage: http://cpb.iphy.ac.cn; http://iopscience.iop.org/cpb

What follows is a list of articles you may be interested in

High-order Bragg forward scattering and frequency shift of low-frequency underwater acoustic field by moving rough sea surface

Ya-Xiao Mo(莫亚枭), Chao-Jin Zhang(张朝金), Li-Cheng Lu(鹿力成), Qi-Hang Sun(孙启航), and Li Ma(马力)
Chin. Phys. B, 2024, 33 (**3**): 034301. DOI: 10.1088/1674-1056/ad108f

Three-dimensional coupled-mode model and characteristics of low-frequency sound propagation in ocean waveguide with seamount topography

Ya-Xiao Mo(莫亚枭), Chao-Jin Zhang(张朝金), Li-Cheng Lu(鹿力成), and Sheng-Ming Guo(郭圣明)
Chin. Phys. B, 2022, 31 (**8**): 084301. DOI: 10.1088/1674-1056/ac538f

Acoustic multipath structure in direct zone of deep water and bearing estimation of tow ship noise of towed line array

Zhi-Bin Han(韩志斌), Zhao-Hui Peng (彭朝晖), Jun Song(宋俊), Lei Meng(孟雷), Xiu-Ting Yang(杨秀庭), and Bing Su(苏冰)
Chin. Phys. B, 2022, 31 (**5**): 054301. DOI: 10.1088/1674-1056/ac364e

Measuring orbital angular momentum of acoustic vortices based on Fraunhofer's diffraction

Chao-Fan Gong(龚超凡), Jing-Jing Li(李晶晶), Kai Guo(郭凯), Hong-Ping Zhou(周红平)†, and Zhong-Yi Guo(郭忠义)‡
Chin. Phys. B, 2020, 29 (**10**): 104301. DOI: 10.1088/1674-1056/ab9c11

Second harmonic magnetoacoustic responses of magnetic nanoparticles in magnetoacoustic tomography with magnetic induction

Gepu Guo(郭各朴), Ya Gao(高雅), Yuzhi Li(李禹志), Qingyu Ma(马青玉), Juan Tu(屠娟), Dong Zhang(章东)
Chin. Phys. B, 2020, 29 (**3**): 034302. DOI: 10.1088/1674-1056/ab6843

Analysis and measurement of vibration characteristics of a hollowing defect based on a laser self-mixing interferometer

Yu-Xin Chen(陈煜昕)[1], Jin-Bo Chen(陈金波)[1,†], Peng Cao(曹鹏)[1], You-Guang Zhao(赵有光)[2,‡], Jun Wang(王钧)[1], Xu-Wei Teng(滕旭玮)[3], and Chi Wang(王驰)[1,§]

[1] *School of Mechatronic Engineering and Automation, Shanghai University, Shanghai* 200072, *China*
[2] *Department of Orthopedics, Shanghai Tongji Hospital, School of Medicine, Tongji University, Shanghai* 200065, *China*
[3] *Shanghai Ideal Information Industry (Group) Co., Ltd., Shanghai* 201315, *China*

(Received 12 June 2024; revised manuscript received 11 September 2024; accepted manuscript online 24 September 2024)

To solve the problems with the existing methods for detecting hollowing defects, such as inconvenient operation, low efficiency and intense subjectivity, and to improve the efficiency of the acoustic-optic fusion method for detecting hollowing defects, in this paper the vibration characteristics of hollowing defects are measured and analyzed using a laser self-mixing interferometer. The ceramic tile above the hollowing defect is equivalent to a thin circular plate with peripheral fixed support. According to Kirchhoff's classical circular plate theory and the circular plate displacement function based on the improved Fourier series, a theoretical model of a circular plate is established. By solving the characteristic equation, the theoretical modal parameters of hollowing defects are obtained. Subsequently, an experimental system based on a laser self-mixing interferometer is built, and modal experiments are carried out using the hammering method. The experimental modal parameters are obtained with a professional modal analysis software. Through comparative analysis between the theoretical and experimental modal parameters, the error of the natural frequency results is found to be tiny and the mode shapes are consistent. These results provide theoretical guidance for a practical non-destructive acoustic-optic fusion method for detecting hollowing defects.

Keywords: hollowing defect, Kirchhoff's classical theory of circular plate, laser self-mixing interference, hammering method, modal

PACS: 43.40.+s, 06.30.Ft, 42.87.–d **DOI:** 10.1088/1674-1056/ad7e99

1. Introduction

During the construction of significant infrastructure (e.g., large bridges and tunnels), problems such as material quality and construction techniques can result in hollowing defects within the structures. A hollowing defect typically refers to the presence of gaps or inadequate bonding between the surface of the structural wall and the base layer. The base layer of the wall undergoes gradual aging over time, amplifying the instability caused by the presence of hollowing defects. Severe cases may lead to structural collapse, posing a significant threat to human life and the safety of property.[1–3] Hence, the development of rational and efficient methods for detecting hollowing defects is imperative.

Currently, there are several methods that are commonly employed to detect hollowing defects: the visual inspection method,[4,5] which involves assessing the presence of hollowing defects by observing cracks inside the wall; the ultrasonic inspection method,[6,7] which relies on measuring linear and nonlinear ultrasonic parameters to determine the presence of defects; and the infrared thermal imaging testing method,[8–11] which entails heating the exterior wall surface and using instruments to detect the temperature distribution, thereby identifying the presence of hollowing defects. However, the interpretation of infrared imaging results is contingent upon the judgment of trained professionals and more objective standards are needed. As well as the methods mentioned above, another commonly employed technique is tap inspection.[12,13] The inspector uses a special hammer to tap the wall surface, assessing the presence of hollowing defects based on the sound produced. While this method is operationally straightforward, it relies heavily on the experience of skilled professionals and is significantly influenced by subjective factors. Each of these techniques has its own characteristics but also exhibits limitations. To ensure that no secondary damage is caused to the structure during detection, and to reduce the risk of damage to the base layer, it is more appropriate to use non-destructive methods for detecting hollowing defects. Therefore, researchers and engineers are continually striving to explore more advanced, convenient and effective non-destructive testing methods for hollowing defects.

In the field of non-destructive detection of buried landmines, a non-destructive acoustic-optic fusion detection method based on the principle of sound resonance has been studied and developed in recent years. Sabatier *et al.* employed laser Doppler technology to detect buried landmines,

†Corresponding author. E-mail: jbchen@shu.edu.cn
‡Corresponding author. E-mail: zhaoyouguang@tongji.edu.cn
§Corresponding author. E-mail: wangchi@shu.edu.cn

© 2024 Chinese Physical Society and IOP Publishing Ltd

analyzing the acoustic resonance characteristics of different types of landmines through experiments. Their results demonstrate the detectability of buried landmines.[14,15] Donskoy *et al.* investigated the 'soil-mine' nonlinear resonance model and analyzed the theoretical nonlinear resonance characteristics. Then, they validated a nonlinear measurement method for buried landmines through experiments.[16–21] Zagrai *et al.* revealed the multi-modal vibration characteristics of buried landmines and analyzed the influence of burial depth and soil moisture on the measurement results.[22–24] Copenhaver *et al.* studied the detection of buried landmines using the off-source pulse method, employing two sets of pulses to excite buried landmines and a seismometer to detect vibration signals.[25] In recent years, the research team led by Wang Chi has conducted research on the theoretical analysis and experimental testing of an acoustic-optic fusion method for detecting landmines based on previous studies.[26–32]

The above research results demonstrate the superiority and reliability of the acoustic-optic fusion detection method and show good prospects in the field of non-destructive testing. This paper introduces the acoustic-optic fusion method into the field of hollowing defect detection. In the area where the hollowing defect exists, the vibration of the ceramic tile surface will be more obvious than in areas with no hollowing defects when sound waves of a certain frequency are used to excite the wall. High-precision optical instruments are employed to detect the information on ceramic tile surface vibrations. When the excitation sound wave frequency is consistent with the natural frequency of the ceramic tile above the hollowing defect, resonance will occur, the vibration amplitude will be the most obvious and the detection efficiency will be the highest. Therefore, the key issue in acoustic-optic fusion detection technology is to study the resonance problem of the hollowing defect structure, that is, to study the vibration characteristics of the hollowing defect.

This paper measures the vibration characteristics of hollowing defects based on the laser self-mixing interference method. This method is widely used to measure physical quantities such as displacement, acceleration, vibration mode, etc. due to its advantages of good stability, high sensitivity, simple optical path and high measurement accuracy. In 1995 Donati *et al.* employed self-mixing technology to achieve displacement measurement, and in 2003 they designed a vibrometer based on the laser self-mixing interference effect.[33–35] In 1988 Groot *et al.* proposed the three-mirror Fabry–Pérot cavity model for analyzing the self-mixing phenomenon and in 1990 they designed a multi-mode semiconductor laser self-mixing interference ranging system.[36,37] Bosch *et al.* used self-mixing technology to achieve the reconstruction of three-dimensional objects. In 2010, they improved the laser self-mixing measurement method to increase the accuracy of displacement measurement.[38,39] Wang *et al.* proposed an improvement to the self-mixing method that combines multiple reflections with phase modulation to achieve displacement reconstruction and improve measurement accuracy.[40] Xie *et al.* introduced phase-shifted fiber Bragg gratings into self-mixing interference technology to enhance the measurement signals and analyze the enhancement effects of surfaces with different reflectivity by comparing the results of simulations and experiments.[41] Zhen *et al.* proposed a vibration measurement algorithm for a self-hybrid system based on Lissajous graph convergence and verified the accuracy of the algorithm through experiments and simulations.[42]

In summary, the technology for detecting hollowing defects has been continuously researched and developed. However, there are few effective detection methods, and no detection methods produce comprehensive and in-depth structural information on hollowing defects. This paper introduces the acoustic-optic fusion detection method into the field of non-destructive detection of hollowing defects, and comprehensively and deeply investigates the structural information and vibration characteristics of the hollowing defect. On the basis of theoretical research, an experimental research framework for measuring the vibration characteristics of hollowing defects based on a laser self-mixing interferometer is established.

2. Problem statement

A hollowing defect can be described as a wall that contains a cavity or defect, as shown in Fig. 1. In the area where the hollowing defect exists, the ceramic tile above the hollowing defect can be equivalent to thin plates with peripheral fixed support, and the shape of the thin plate is determined by the shape of the hollowing defect. Taking the circular hollowing defect studied in this paper as an example, the ceramic tile above the hollowing defect is equivalent to a circular thin plate with peripheral fixed support.

Research on the vibration characteristics of hollowing defect structures has a crucial role in the development of actual technology for detecting hollowing defects. By analyzing the modal parameters such as the natural frequency and modal shape of the hollowing defect structures, the vibration rules for the hollowing defect structures can be thoroughly investigated, greatly improving the efficiency of hollowing defect detection. This analysis process is termed modal analysis. Modal analysis can be divided into theoretical modal analysis and experimental modal analysis. Theoretical modal analysis refers to establishing a model of the structure based on dynamic equations and employing finite-element calculations to obtain the modal parameters of the hollowing defect. Experimental modal analysis refers to obtaining the excitation and response of the structure by applying external excitation, and

obtaining the modal parameters through parameter identification.

To explore an efficient and accurate method for detecting hollowing defects and provide a theoretical basis for the acoustic-optic fusion detection method, the work described in this paper combines theoretical analysis with experimental research into the vibration information from hollowing defects. Based on Kirchhoff's classical plate theory, a theoretical model of a circular plate vibration system is established and the natural frequencies and mode shapes of the structures under specific boundary conditions are obtained. Additionally, an experimental modal test based on a laser self-mixing interferometer is conducted to obtain the experimental modal parameters. By comparing the theoretical and experimental results, the rationality and effectiveness of the proposed method are validated.

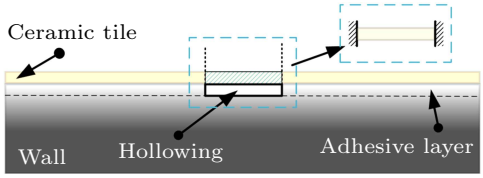


Fig. 1. Schematic diagram of a hollowing defect.

3. Theoretical modal analysis

According to Kirchhoff's classical theory of a circular plate, the radial displacement component $u(r,\theta)$ and the tangential displacement component $v(r,\theta)$ at any arbitrary point within the circular plate can be expressed as

$$\begin{cases} u(r,\theta) = -z\dfrac{\partial w(r,\theta)}{\partial r}, \\ v(r,\theta) = -\dfrac{z}{r}\dfrac{\partial w(r,\theta)}{\partial \theta}, \end{cases} \tag{1}$$

where $w(r,\theta)$ is the displacement function of the circular plate.

In cylindrical coordinates, based on the geometric deformation conditions of the circular plate and the generalized Hooke's law, the stress–strain equation of circular plate vibration can be derived as

$$\Rightarrow \begin{cases} \sigma_r = \dfrac{E}{1-\mu^2}(\varepsilon_r + \mu\varepsilon_\theta), \\ \sigma_\theta = \dfrac{E}{1-\mu^2}(\varepsilon_\theta + \mu\varepsilon_r), \\ \tau_{r\theta} = \dfrac{E}{2(1+\mu)}\gamma_{r\theta}, \end{cases} \tag{2}$$

where ε_r is the radial strain, ε_θ is the tangential strain and $\gamma_{r\theta}$ is the angular strain. σ_r, σ_θ and $\tau_{r\theta}$ represent radial stress, tangential stress and shear stress, respectively, μ is Poisson's ratio and E is the elastic modulus of the material.

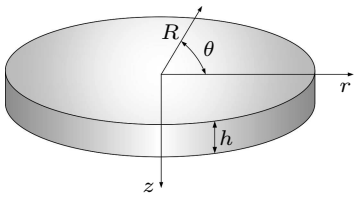


Fig. 2. Schematic diagram of the structure of a circular plate in cylindrical coordinates.

When considering the vibration of a circular plate, the internal interactions within the circular plate are taken into account. Consequently, a differential unit body is selected for mechanical analysis, as depicted in Fig. 3.

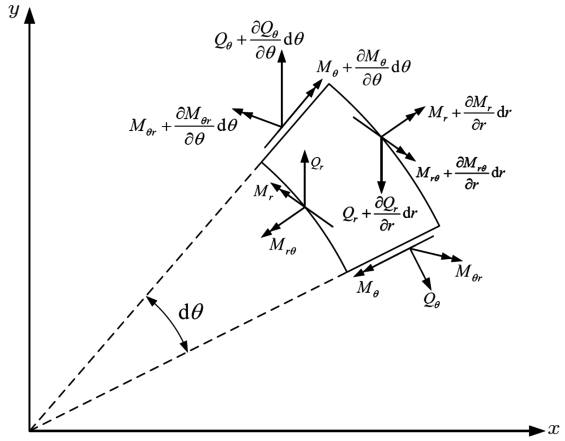


Fig. 3. Force diagram inside a round plate.

The bending moments M_r, M_θ and $M_{r\theta}$ are obtained by integrating the stresses σ_θ, σ_r and $\tau_{r\theta}$ along the z direction, respectively, for each point. According to the theorem of conjugate shear stress, $M_{\theta r} = M_{r\theta}$. Their expressions are given as follows:

$$M_r = \int_{-\frac{h}{2}}^{\frac{h}{2}} \sigma_r z \mathrm{d}z = -D\left[\frac{\partial^2 w(r,\theta)}{\partial r^2} + \mu\left(\frac{1}{r}\frac{\partial w(r,\theta)}{\partial r} + \frac{1}{r^2}\frac{\partial^2 w(r,\theta)}{\partial \theta^2}\right)\right], \tag{3a}$$

$$M_\theta = \int_{-\frac{h}{2}}^{\frac{h}{2}} \sigma_\theta z \mathrm{d}z = -D\left[\left(\frac{1}{r}\frac{\partial w(r,\theta)}{\partial r} + \frac{1}{r^2}\frac{\partial^2 w(r,\theta)}{\partial r^2}\right) + \mu\frac{\partial^2 w(r,\theta)}{\partial r^2}\right], \tag{3b}$$

$$M_{r\theta} = M_{\theta r} = \int_{-\frac{h}{2}}^{\frac{h}{2}} \tau_{r\theta} z \mathrm{d}z = -D(1-\mu)\frac{\partial}{\partial r}\left(\frac{1}{r}\frac{\partial w(r,\theta)}{\partial r}\right), \tag{3c}$$

where $D=\frac{Eh^3}{12(1-\mu^2)}$ is the bending rigidity of the circular plate.

Based on the schematic diagram illustrating the interactions of the differential unit body, the dynamic equations of the system can be derived as

$$\frac{\partial M_r}{\partial r}+\frac{1}{r}\frac{\partial M_{r\theta}}{\partial r}-Q_r=0, \tag{4a}$$

$$\frac{\partial M_{r\theta}}{\partial r}+\frac{1}{r}\frac{\partial M_{\theta}}{\partial \theta}-Q_\theta=0, \tag{4b}$$

$$\frac{\partial Q_r}{\partial r}+\frac{1}{r}\frac{\partial Q_\theta}{\partial \theta}-\rho h\frac{\partial^2 w}{\partial t^2}=0, \tag{4c}$$

where ρ is the mass density of the material and h is the thickness of the circular plate. By substituting Eqs. (3a)–(3c) into Eqs. (4a)–(4c), the expressions for Q_r and Q_θ can be obtained as

$$Q_r=-D\frac{\partial}{\partial r}\left[\frac{\partial^2 w(r,\theta)}{\partial r^2}+\frac{1}{r}\frac{\partial w(r,\theta)}{\partial r}+\frac{1}{r^2}\frac{\partial^2 w(r,\theta)}{\partial \theta^2}\right], \tag{5a}$$

$$Q_\theta=-\frac{D}{r}\frac{\partial}{\partial \theta}\left[\frac{\partial^2 w(r,\theta)}{\partial r^2}+\frac{1}{r}\frac{\partial w(r,\theta)}{\partial r}+\frac{1}{r^2}\frac{\partial^2 w(r,\theta)}{\partial \theta^2}\right]. \tag{5b}$$

Through Eqs. (4a)–(4c), (5a) and (5b), the dynamic equation for the circular plate can be derived as

$$\begin{aligned}&\left(\frac{\partial^2}{\partial r^2}+\frac{\partial}{r\partial r}+\frac{\partial^2}{r^2\partial\theta^2}\right)\\&\times\left(\frac{\partial^2 w(r,\theta)}{\partial r^2}+\frac{\partial w(r,\theta)}{r\partial r}+\frac{\partial^2 w(r,\theta)}{r^2\partial\theta^2}\right)\\&+\frac{\rho h}{D}\frac{\partial^2 w(r,\theta)}{\partial t^2}=0.\end{aligned} \tag{6}$$

By employing the Laplace operator $\nabla^2=\left(\frac{\partial^2}{\partial r^2}+\frac{\partial}{r\partial r}+\frac{\partial^2}{r^2\partial\theta^2}\right)$, Eq. (6) can be simplified as

$$D\nabla^2\nabla^2 w(r,\theta)-\rho h\omega^2 w=0, \tag{7}$$

where w is the deflection of the circular plate and ω is the circular frequency of the system.

The configuration of boundary conditions is achieved by distributing lateral constraint springs and torsional springs around the periphery of the circular plate. As depicted in Fig. 4, K and k are the stiffness values of springs. Simulation of different boundary conditions is accomplished by modifying the stiffness values of the corresponding springs.

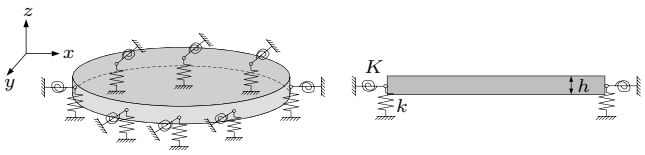


Fig. 4. Theoretical model of circular plate vibration.

Based on the vibration theory model established in this paper for a circular plate, the boundary conditions can be described as

$$\begin{aligned}kw(r,\theta)&=-D\frac{\partial}{\partial r}\nabla^2 w(r,\theta),\\K\frac{\partial w(r,\theta)}{\partial r}&=-D\left[\frac{\partial^2 w(r,\theta)}{\partial r^2}\right.\\&\left.+\mu\left(\frac{1}{r}\frac{\partial w(r,\theta)}{\partial r}+\frac{1}{r^2}\frac{\partial^2 w(r,\theta)}{\partial\theta^2}\right)\right].\end{aligned} \tag{8}$$

In cylindrical coordinates, the displacement function for a circular plate based on the improved Fourier series method can be denoted as

$$w(r,\theta)=\sum_{m=0}^{M}A_m f_m(r)\cos(n\theta),\quad n=1,2,\ldots,N, \tag{9}$$

where A_m is the undetermined expansion coefficient of the unknown Fourier series in the displacement function. M and N are the truncation orders in the series expansion. In a physical context, M corresponds to the number of pitch circles and N corresponds to the number of pitch diameters. For any function $w(r,\theta)$, as the number of truncation orders increases the accuracy of the solution improves. These results can achieve arbitrary precision in theory. $f_m(r)$ is the displacement function employed to enhance convergence and solution accuracy, and is expressed as follows:

$$f_m(r)=\begin{cases}\sin(\lambda_m r), & m=1,2,3,4,\\ \cos(\lambda_{(m-5)}r), & m\geq 5,\end{cases} \tag{10}$$

where $\lambda_m=\frac{m\pi}{R}$, with R being the radius of the circular plate.

According to the theoretical model established in Fig. 4, the total energy of the system, L, of the circular plate is defined as $L=U+V-T$, where U is the strain energy of the circular plate, V is the potential energy of the springs and T is the total kinetic energy of the system. The expressions are as follows:

$$\begin{aligned}U=&\frac{D}{2}\int_0^{2\pi}\int_0^{R}\left\{\left(\frac{\partial^2 w(r,\theta)}{\partial r^2}+\frac{\partial w(r,\theta)}{r\partial r}+\frac{\partial^2 w(r,\theta)}{r^2\partial\theta^2}\right)^2\right.\\&-2(1-\mu)\left[\frac{\partial^2 w(r,\theta)}{\partial r^2}\left(\frac{\partial w(r,\theta)}{r\partial r}+\frac{\partial^2 w(r,\theta)}{r^2\partial\theta^2}\right)\right.\\&\left.\left.-\left(\frac{\partial w(r,\theta)}{r\partial r\partial\theta}+\frac{\partial^2 w(r,\theta)}{r^2\partial\theta}\right)\right]\right\}r\mathrm{d}r\mathrm{d}\theta,\end{aligned} \tag{11a}$$

$$V=\frac{R}{2}\int_0^{2\pi}\left[kw^2(r,\theta)+K\left(\frac{\partial w(r,\theta)}{\partial r}\right)^2\right]_{r=R}\mathrm{d}\theta, \tag{11b}$$

$$T=\frac{1}{2}\rho h\int_0^{2\pi}\int_0^{R}w(r,\theta)r\mathrm{d}r\mathrm{d}\theta. \tag{11c}$$

Substituting Eqs. (11a)–(11c) into the total energy expression for the system, the Rayleigh–Ritz method is employed to solve the extreme value of undetermined coefficients A_m in the displacement function. This yields a linear system of equations concerning the expansion coefficients of the unknown series, represented as follows:

$$\left(\boldsymbol{K}-\omega^2\boldsymbol{M}\right)\boldsymbol{A}=0, \tag{12}$$

where $\boldsymbol{K}$ is the stiffness matrix, $\boldsymbol{M}$ is the mass matrix and $\boldsymbol{A}$ is the vector of the undetermined coefficients.

Equation (12) is a linear homogeneous equation system and the coefficient vector $\boldsymbol{A}$ is not zero. According to Cramer's rule, the system characteristic equation can be obtained by

$$\left|\boldsymbol{K}-\omega^2\boldsymbol{M}\right|=0. \tag{13}$$

The characteristic Eq. (13) is solved using scientific computing software. When solving characteristic equations, each eigenvalue corresponds to a natural frequency and the order of the eigenvalue is also the order of the natural frequency. Each natural frequency corresponds to an eigenvector, which reflects the mode shape information of the structure. When a sound wave of a certain frequency is applied to excite the structure, the structure undergoes deformation. When the deformation is maximum, the frequency corresponds to the natural frequency of the structure itself. As the natural frequency increases, the corresponding eigenvectors decrease, meaning that the vibration amplitude of the structure is smaller.

4. Experimental system design

4.1. Overview of modal experiment system

The objective of the experiment in this paper is the detection of hollowing defects of different sizes. Due to the advantages of its simple operation and accuracy, the hammering method is employed in this paper to conduct a modal testing experiment.

By arranging impact force points on the surface of the ceramic tile above the hollowing defect, a modal testing force hammer is used to apply stable dynamic excitation to each point. Subsequently, a laser Doppler vibrometer emits a laser beam towards the ceramic tile surface and captures the vibration response signals.

According to the Maxwell reciprocity theorem, the response at point p caused by an input at point q in the structure is equal to the response at point q caused by the same input at point p. Therefore, the center point of the ceramic tile above the hollowing defect is set as a fixed response point, and the vibration signals collected at this point are also the vibration signals when tapping each point.

The collected force signals and response signals are processed by the modal identification algorithm to obtain the corresponding experimental modal parameters. Based on this principle, an experimental system for determining the hollowing defect vibration characteristics was designed, and is shown in Fig. 5. The test system comprises a force hammer, a laser Doppler vibrometer, a mobile workstation and a data collector.

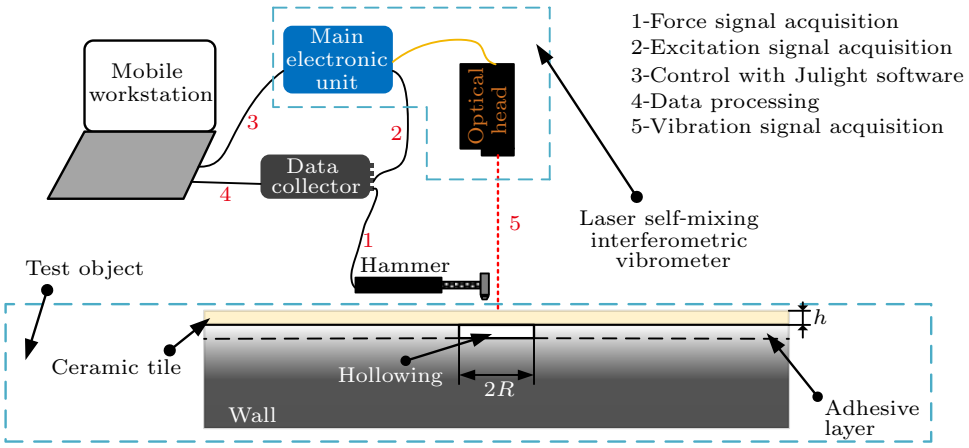


Fig. 5. Schematic diagram of the test system.

4.2. Performance parameters of the instrument

The force hammer employed in the experimental system is an 086C03 pulse hammer produced by PCB Piezotronics, Inc., USA. The laser Doppler vibrometer is a VSM1000L series manufactured by Julight Srl, Italy. The laser vibrometer is designed

Table 1. Main performance parameters of the instruments.

Force hammer	VSM-DAQ-4	VSM1000 series	
Sensitivity (±15%) 2.25 mV·N^{-1}	Input channels 4	Working distance	0.1–5 m
Range ±220 N·pk	Output channels 1	Measurable vibration frequencies	DC, 3 MHZ
Resonant frequency ≥ 22 kHz	Analog/digital resolution 24 bps	Laser spot size	100 μm
Linearity ≤ 1	Maximum sampling frequency 80 kHz	Minimum displacement resolution	10 pm
		Laser head size	50 mm×70 mm×105 mm
		Main electronic unit size	12.5 cm×15.5 cm×29.6 cm
		Wavelength	Class 1M 1310 nm (invisible) Class II 650 nm (visible)

on the principle of self-mixing interference, and offers advantages such as a compact footprint, simple structure, easy optical alignment, convenient installation and high reliability. It enables precise non-contact detection of vibration signals on rough surfaces. The data collector is a VSM-DAQ-4, also produced by Julight Srl. It can be easily adapted to the VSM series vibrometers. The data collector features robust computational capabilities for accurate capture of both force signals and minute vibration signals. The key performance parameters are listed in Table 1.

4.3. Hammering method test system

A schematic diagram of the hollowing defect modal analysis experimental system is shown in Fig. 6(a).

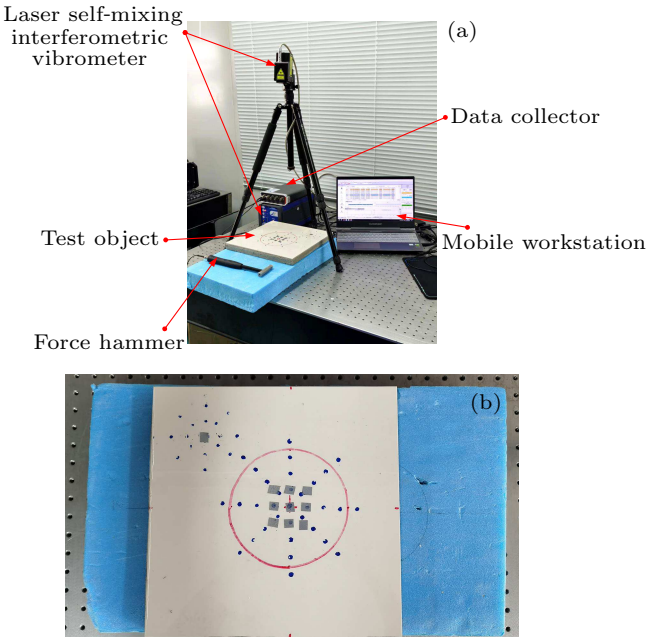


Fig. 6. Hammering method test system: (a) overall experimental diagram and (b) test object.

The object is a wall with a hollowing defect, shown in Fig. 6(b). Distributed impact force points are marked on the surface of the test object. Subsequently, the model of the hollowing defect is established using professional modal analysis software. The specific modeling information for the impact force points is indicated with arrows, as shown in Fig. 7.

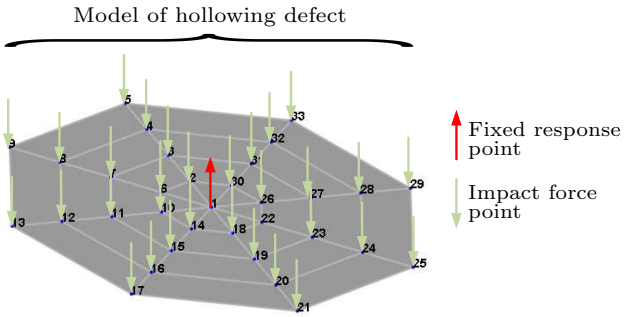


Fig. 7. Measuring points of the hammering method test.

5. Results and discussion

5.1. Theoretical modal parameter — natural frequency

The first and second natural frequencies typically correspond to the most significant vibration modes of the structure. In the vibration characteristic experiment, the measurement of lower-order natural frequencies (especially the first order) is relatively straightforward and yields more reliable results. Measuring higher-order frequencies increases the complexity and uncertainty of the experiment. Therefore, focusing on the analysis of the first and second natural frequencies can provide more accurate assessment of the structural vibration characteristics and is more effective.

By setting relevant parameters, as illustrated in Table 2, the characteristic equation for the circular plate (Eq. (13)) is solved to obtain the natural frequencies of the circular plate with peripheral fixed support. Certainly, throughout the solution process it is imperative to prove the convergence and accuracy of the method to ensure the reliability of the theoretical solution.

Table 2. Main parameters of the ceramic tile.

Material parameters	Elastic modulus = 25×10^9 Pa	Mass density = 2315 kg·m^{-3}	Poisson's ratio = 0.2
Dimension parameters	Thickness h = 0.005 m	Radius R = 0.05–0.06 m	

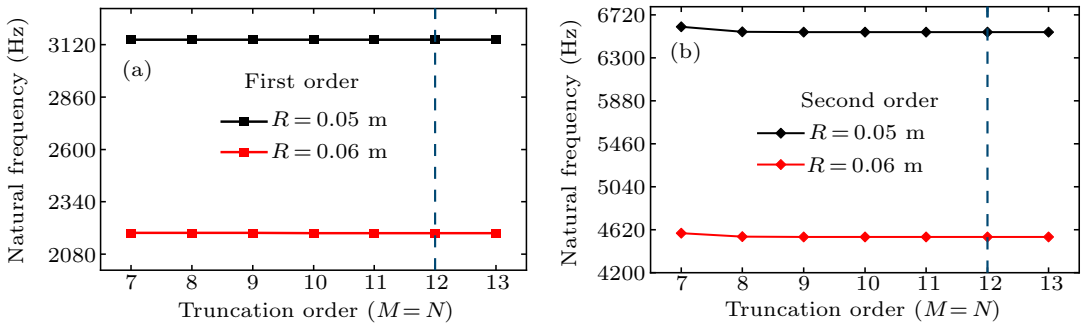


Fig. 8. Natural frequencies at different truncation order: (a) trend of the first-order frequency and (b) trend of second-order frequency.

To verify the convergence of the proposed method, a specified stiffness value is set and the natural frequencies of the characteristic equation are solved under different truncation orders. As depicted in Fig. 8, the natural frequencies with truncation orders $M = N$ ranging between 7 and 13 are listed. It can be observed that the overall trend of the first natural frequency is relatively small, as shown in Fig. 8(a). The second natural frequency exhibits significant variation, ranging from 7 to 10, while it remains nearly constant with a truncation order exceeding 8, as shown in Fig. 8(b).

To facilitate a comparison of the impact of the truncation order on the natural frequency value, the relative errors of the results with different truncation orders are depicted in Table 3. It is observed that the maximum relative error is only -0.75%. When the truncation order is set to 13, the relative error reaches a minimum, indicating that the results have the best convergence and proving that the method proposed in this paper has good numerical stability. Consequently, the truncation order is uniformly set to $M = N = 12$.

Table 3. Relative error at different truncation orders.

Relative error (%)		Truncation order ($M = N$)						
		7	8	9	10	11	12	13
$R = 0.05$ m	First order	–	–0.0016	–0.0200	–0.0051	–0.0029	–0.0035	–0.0013
	Second order	–	–0.7082	–0.0445	–0.0122	–0.0020	–0.0008	–0.0001
$R = 0.06$ m	First order	–	–0.0005	–0.0087	–0.0032	–0.0023	–0.0023	–0.0012
	Second order	–	–0.7532	–0.0437	–0.0132	–0.0020	–0.0007	–0.0002

After confirming the convergence of the characteristic equation, the numerical accuracy of the dynamic equations established in this paper is verified. Theoretically, a peripheral fixed support can be implemented by setting the stiffness value $k = K$ to infinity. However, from a theoretical perspective, the natural frequency values will converge as the stiffness value approaches a certain threshold. Further increasing the stiffness value will only extend the computational solving time.

Therefore, stiffness values of $k = K = 10^7$, 10^8, 10^9, 10^{10}, 10^{11} and 10^{12} are selected, and the natural frequencies with these different stiffness values are obtained. The results are compared as shown in Fig. 9.

As the stiffness value varies, it can be observed in Fig. 9 that the solutions change significantly, and the second-order natural frequency as shown in Fig. 9(b) experiences a more extensive range of change than the first-order natural frequency (Fig. 9(a)). However, the natural frequency values converge when the stiffness value exceeds 10^{10} or higher.

In the same way, to facilitate a more intuitive comparison of the influence of stiffness values on the natural frequencies, Table 4 lists the relative errors of circular plates with different radii under spring constraints with various stiffness values. It is evident that when the stiffness value of the spring constraint is set to 10^{13}, the relative error reaches its minimum, resulting in the most accurate solutions. Hence, the stiffness value of the spring constraint is uniformly set to $k = K = 10^{12}$ for the numerical calculations in this paper.

The values of spring stiffness and truncation order are determined, and theoretical solutions of the natural frequencies are obtained. The modal analysis simulation of the circular plate is carried out using finite-element software to obtain the numerical simulation result. Table 5 lists the results.

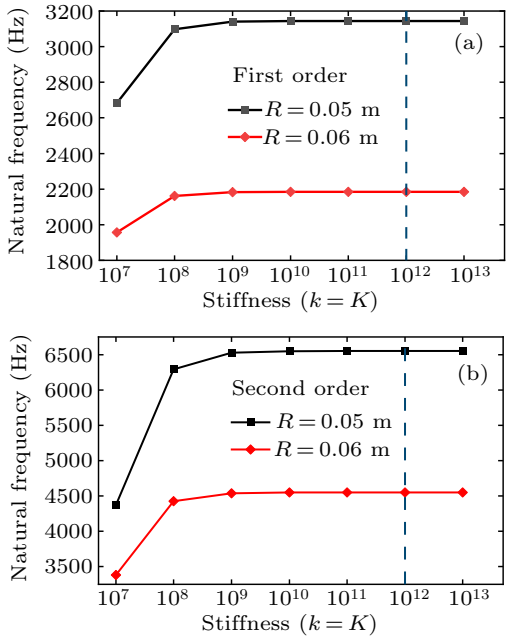


Fig. 9. Natural frequencies at different stiffness values: (a) first-order frequency change trend and (b) second-order frequency change trend.

Table 4. Relative error at different stiffness values.

Relative error (%)		Stiffness ($k = K$)						
		10^7	10^8	10^9	10^{10}	10^{11}	10^{12}	10^{13}
$R = 0.05$ m	First order	–	15.4247	1.3757	0.1354	0.0134	0.0013	0.0003
	Second order	–	43.9445	3.7312	0.3504	0.0348	0.0034	0.0005
$R = 0.06$ m	First order	–	10.4393	0.9511	0.0939	0.0096	0.0009	0.0000
	Second order	–	30.7832	2.5393	0.2426	0.0242	0.0024	0.0002

Table 5. Theoretical prediction versus numerical simulation.

Frequency (Hz)	$R = 0.05$ m		Error (%)	$R = 0.06$ m		Error (%)
	Theoretical solution	Numerical simulation		Theoretical solution	Numerical simulation	
First order	3144.58	3077.7	2.2	2184.6	2151.9	1.5
Second order	6552.2	6271.4	4.5	4550.16	4411.7	3.1

The results in Table 5 show that the maximum error of the natural frequencies is within 5%, which verifies the rationality of the vibration theoretical model based on Kirchhoff's classical plate theory. Subsequently, the modal analysis experiment for the hollowing defect is established to verify the effectiveness of our proposed method.

5.2. Experimental results and discussion

During the experimental process of using the hammering method to obtain the modal parameters, the issue of multiple hits may occur. Multiple hits will generate multiple pulse signals, as shown in Fig. 10(a), and cause distortion of the force spectrum. Additionally, they will produce an irregular force spectrum curve, as shown in Fig. 10(b). A distorted force spectrum cannot accurately reflect the actual force signal, affecting the extraction of modal parameters. Therefore, it is essential to avoid multiple hits during the experiment.

Proper hammering excitation will only generate a single pulse signal, and the force spectrum is relatively smooth, as shown in Figs. 10(c) and 10(d).

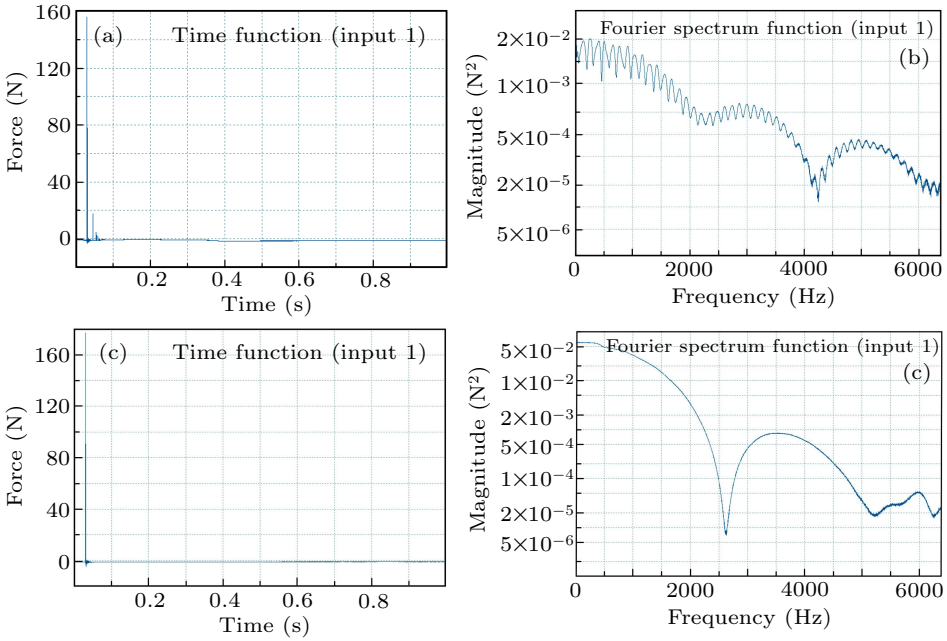


Fig. 10. Force signal: (a) time function of multiple hits; (b) spectrum function of multiple hits; (c) time function of a proper hit; (d) spectrum function of a proper hit.

After ensuring that the pulse force signal of each excitation point is correct, the excitation signal and response signal are collected by the data collector and then input to the mobile workstation. The vibration signals are generated by tapping the surface of the ceramic tile above the hollowing defect with a force hammer. The vibration displacement signal of each excitation point is obtained through a laser self-mixing interferometer and transmitted to the computer via the data collector. The modal parameter of the hollowing defect structure can be obtained through data processing with professional modal analysis software.

According to the above experimental testing method, the modal parameters of walls with hollowing defects are obtained with radii of 0.05 m and 0.06 m. We will also compare the modal characteristic with no hollowing defect inside the wall. Subsequently, a comparative analysis of these results was conducted. As evident from the results listed in Table 5, the first-order natural frequency values all exceed 2000 Hz, which are medium–high frequencies, while the second-order natural frequency values are higher. Considering the influence of hardware factors, and referring to the force spectrum information, the high-frequency vibration response signals will be distorted. Therefore, here we focus on analysis of the first-order natural frequency, which is also the matter of most concern in subsequent actual detection work.

The modal indicator function curve of a hollowing defect structure with a radius of 0.06 m is depicted in Fig. 11. The curve exhibits prominent peaks. The peak point occurs at a frequency of 2208 Hz, with an amplitude of −54.2 dB. It can be observed that the curve does not display an obvious

peak near the theoretical value of the second-order natural frequency, which also verifies the accuracy of the above analysis. To verify whether the frequency value at the peak point corresponds to the natural frequency it is necessary to analyze the corresponding mode shape at the peak point.

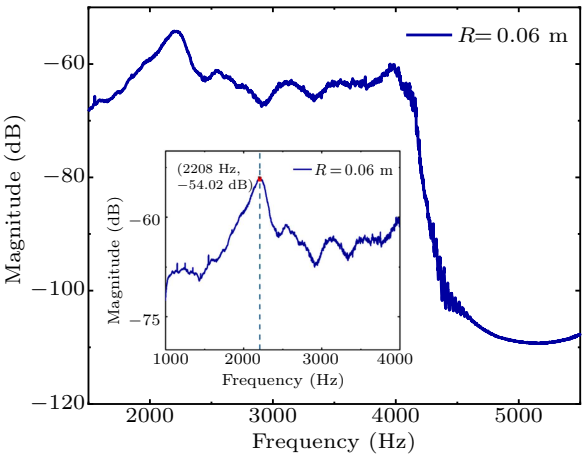


Fig. 11. Modal indicator function curve ($R = 0.06$ m).

The experimental mode shape corresponding to the peak point is depicted in Fig. 12. It can be observed that the amplitude changes in the central area of the mode shape are more obvious, while the amplitude changes at the edge of the hollowing defect are relatively small. The overall mode shape is symmetrical. The experimental vibration shapes are compared with the theoretical solutions and simulation solutions. A comparative analysis is conducted between the experimental mode shape and the theoretical modal shape as well as the simulated mode shape.

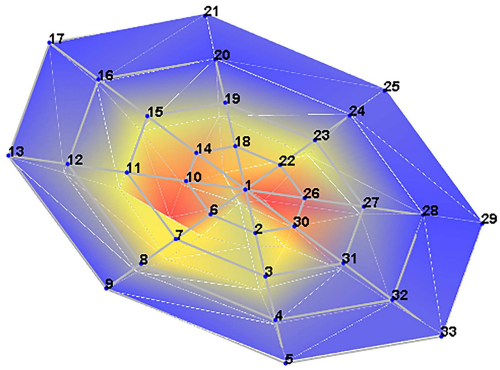


Fig. 12. Mode shape of the top point ($R = 0.06$ m).

By substituting the eigenvector corresponding to the theoretical solution of natural frequency into the system displacement function, the theoretical mode shape of the hollowing defect structure can be obtained, as shown in Fig. 13(a). Simulated mode shapes can be obtained through post-processing using finite-element software, as shown in Fig. 13(b).

As shown in Fig. 13, in conjunction with the experimental mode shape shown in Fig. 12, the experimental mode shape corresponding to the peak point is consistent with the theoretical mode shape and the simulated vibration shape of the first-order natural frequency. It can be proved that the frequency corresponding to the peak point is the first-order natural frequency of a hollowing defect structure with a radius of 0.06 m.

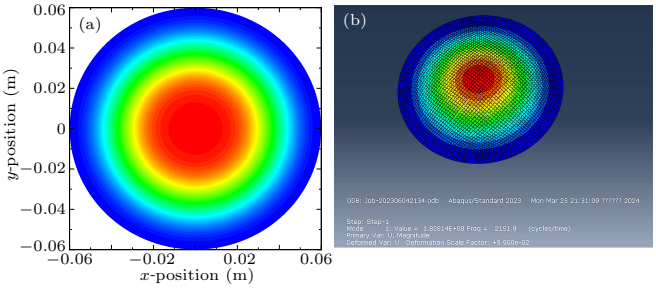


Fig. 13. Mode shape of first order natural frequency ($R = 0.06$ m): (a) theoretical mode shape; (b) simulated mode shape.

Next, the modal parameters of a hollowing defect with a radius of 0.05 m are analyzed. The modal indicator function curve is depicted in Fig. 14. Two prominent peak points are observed in the figure. The first peak point (T1) occurs at a frequency of 2832 Hz with a vibration magnitude of −41 dB. The second peak (T2) occurs at a frequency of 3160 Hz with a vibration magnitude of −54.15 dB. The natural frequency of the structure cannot be determined through numerical results, so it is also necessary to compare the actual mode shapes corresponding to the two peak points.

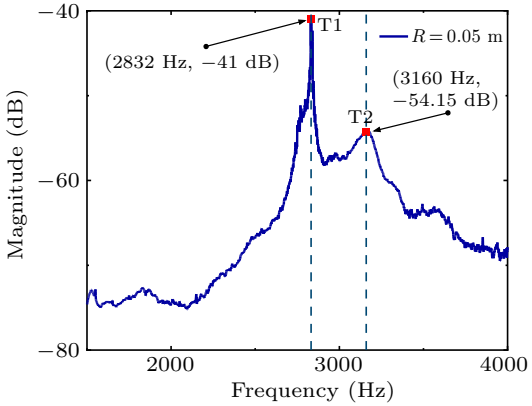


Fig. 14. Modal indicator function curve ($R = 0.05$ m).

Figure 15 shows the mode shapes corresponding to the two peak points. It is evident that the mode shape corresponding to peak point T1 does not have a symmetrical shape in the central area, and there is a local and noticeable amplitude change at excitation point 8. This is because it cannot be guaranteed that all parameters are consistent during the experiment, and the test object cannot reach the most ideal state when it is produced. However, combined with the mode shape in Fig. 15(a), it can be inferred that the frequency corresponding to peak point T1 is not the natural frequency. Conversely, as shown in Fig. 15(b), the mode shape corresponding to peak point T2 is more consistent with the mode shape of the first-order natural frequency.

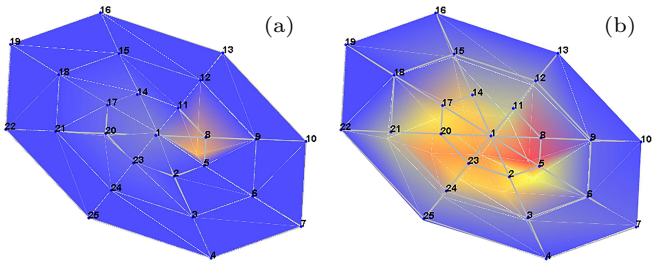


Fig. 15. Mode shape of the top point ($R = 0.05$ m): (a) T1 point; (b) T2 point.

In the same way, the experimental mode shape corresponding to peak point T2 is also consistent with the theoretical mode shape and the simulated vibration shape of the first-order natural frequency shown in Fig. 16. It can be inferred that the frequency corresponding to peak point T2 is the first-order natural frequency of a hollowing defect structure with a radius of 0.05 m.

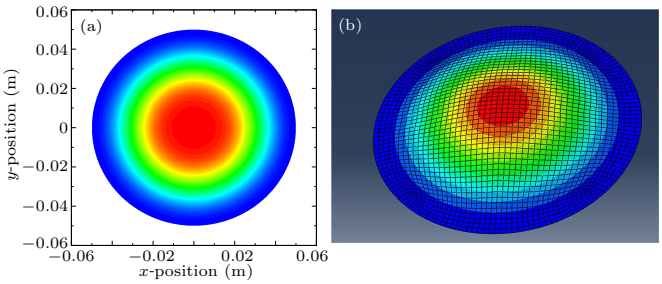


Fig. 16. Mode shape of first order natural frequency ($R = 0.05$ m): (a) theoretical mode shape; (b) simulated mode shape.

After completing the modal analysis of walls with a hollowing defect, we shall also conduct a modal analysis experiment on a wall with no hollowing defect. The results depicted in Fig. 17 are obtained. It can be observed that the obtained modal indicator function curve changes irregularly, with no obvious peak point in the curve. The maximum vibration magnitude of structural variation is −63 dB. The corresponding mode shape at this frequency is shown in Fig. 17(b). It can be observed that the vibration change characteristics of the structure are inconsistent with the vibration change characteristics of a circular plate with peripheral fixed boundary support.

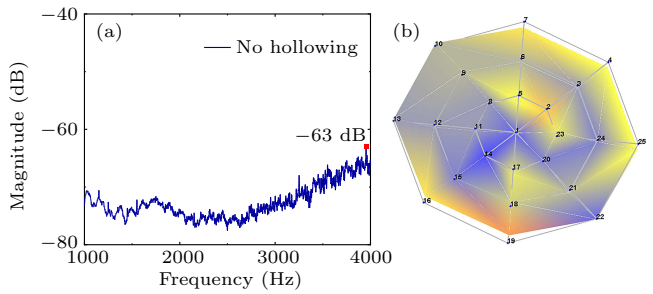


Fig. 17. Experimental modal parameters of the wall without hollowing: (a) modal indicator function curve; (b) mode shape.

The mode reflects the natural vibration characteristics of a structure. Through the above modal analysis, preliminary conclusions can be obtained. The vibration characteristics of walls with a hollowing defect are significantly different from those with no hollowing defect. Under external excitation, when the excitation frequency is consistent with the resonant frequency, the ceramic tile above a hollowing defect will produce obvious deformation, while a structure with no hollowing defect cannot produce such vibration characteristics.

The above analytical results indicate that the vibration information from hollowing defects is consistent with the theoretical derivation proposed in this paper. However, further validation is required to verify whether the natural frequency results coincide with the theoretical solutions. A comparison of the results is listed in Table 6.

Table 6. The error of the results.

Natural frequency (Hz)	$R = 0.05$ m		$R = 0.06$ m	
		Error (%)		Error (%)
Theoretical solution	3144.58	–	2184.6	–
Numerical simulation	3077.7	2.2	2151.9	1.5
Experimental result	3160	–0.5	2208	–1.1

From the results in Table 6 it can be seen that the error between the experimental results and the theoretical solutions is small, which verifies the effectiveness and rationality of the dynamic model of the hollowing defect structure based on Kirchhoff's classical plate theory presented in this paper. Our results can help engineers better understand the vibration information from hollowing defects and greatly improve detection efficiency.

6. Conclusion

In this paper, we conduct modal analysis of hollowing defect structures by employing a laser self-mixing interferometer combined with the hammer method. Taking hollowing defects with radii of 0.05 m and 0.06 m as the research object, the results can provide a technical scheme for actual hollowing defect detection and promote the further development of non-destructive detection technology based on the acoustic-optic fusion method for hollowing defects. Our main findings are as follows:

(1) Based on Kirchhoff's classical circular plate theory, a theoretical model of the hollowing defect structure is established and the characteristic equation of a hollowing defect structure under complex boundary conditions is derived.

(2) The theoretical natural frequencies and modal shapes of hollowing defects are obtained. By comparing the errors between the theoretical solution and numerical simulation of the natural frequency, the rationality of the method proposed in this article is preliminarily verified.

(3) Modal analysis experiments based on a laser self-mixing interferometer combined with the hammer method are conducted and the experimental modal results are compared and analyzed.

(4) The experimental modal parameters are consistent with the theoretical and simulated results. Moreover, the results of experimental modal analysis between a wall with a hollowing defect and a wall with no hollowing defect are analyzed and compared.

Acknowledgements

Project supported by the National Key Research and Development Program of China (Grant No. 2023YFF0722900), the Beijing Engineering Research Center of Aerial Intelligent Remote Sensing Equipments Fund (Grant No. AIRSE20233), and the National Natural Science Foundation of China (Grant No. 62175144).

References

[1] Liao C T 2020 *J. Asian. Archit. Build.* **17** 549
[2] Yiu C Y, Ho D C W and Lo S M 2007 *Constr. Build. Mater.* **21** 594
[3] Zhu B and Zhang H 2014 *Journal of China Three Gorges University (Natural Sciences)* **36** 83
[4] Jiang C J, Shang D F, Zhu Y H and Lu W S 2023 *Construction Technology* **52** 128
[5] Jiang R 2018 *The Research to the Common Quality Issue of Curtain Wall of Buildings and Its Countermeasures* (M.D. Dissertation) (Nanjing: Southeast University) (in Chinese)
[6] Shokouhi P, Wolf J and Wiggenhauser H 2013 *J. Bridge. Eng.* **19** 04013005
[7] Shah A A, Ribakov Y and Zhang C 2013 *Mater. Design.* **50** 905
[8] Datcu S, Ibos L, Candau Y and Matteï S 2005 *Infrared. Phys. Techn.* **46** 451
[9] Lucchi E 2018 *Renew. Sust. Energ.* **82** 3077
[10] Lu Y C, Lin D M, Zhai Z Q and Wang Z S 2022 *Energ. Buildings* **274** 112421
[11] Wang P J, Xiao J Z, Duan Z H and Li C L 2022 *J. Archit. Civil. Eng.* **39** 24
[12] Mccann D M and Forde M C 2001 *NDT & E. Int.* **34** 71
[13] Zhang X Q, Liu W B, Kong G and Gao J W 2017 *Housing Science* **37** 45
[14] Sabatier J M and Xiang N 2001 *IEEE T. Geosci. Remote.* **39** 1146
[15] Xiang N and Sabatier J M 2003 *J. Acoust. Soc. Am.* **113** 1333
[16] Sabatier J M and Xiang N 2000 *Proceedings of Spie the International Society for Optical Engineering*, August 22, 2000, Orlando, FL, United States, p. 4038
[17] Korman M S and Sabatier J M 2004 *J. Acoust. Soc. Am.* **116** 3354
[18] Donskoy D 2004 *J. Acoust. Soc. Am.* **111** 2705
[19] Donskoy D, Reznik A, Zagrai A and Ekimov A 2005 *J. Acoust. Soc. Am.* **117** 690
[20] Donskoy D, Zagrai A, Fenneman D, Tsionskiy M and Sedunov N 2006 *Conference on Detection and Remediation Technologies for Mines and Minelike Targets*, May 17, Orlando, FL, United States, p. 6217
[21] Zabolotskaya E A, Ilinskii Y A and Hamilton M F 2009 *J. Acoust. Soc. Am.* **125** 2035
[22] Zagrai A, Donskoy D and Ekimov A 2004 *Proceedings of Spie the International Society for Optical Engineering*, September 21, 2004, Orlando, FL, United States, p. 5415
[23] Zagrai A, Donskoy D and Ekimov A 2005 *J. Acoust. Soc. Am.* **118** 3619
[24] Muir T G, costley R D and Sabatier J M 2014 *J. Acoust. Soc. Am.* **135** 49
[25] Copenhaver B J, Gorhum J D, Slack C M, Barlett M L and Hamilton M F 2013 *J. Acoust. Soc. Am.* **134** 4129
[26] Wang C, Liu Z G, Li X F, Sun F and Zhang G X 2008 *Acta Acoustica* **33** 354
[27] Wang C, Li X F, Fu J, Li H Y, Liang G Q and Zhang G X 2008 *Optics and Precision Engineering* **16** 1716
[28] Mao X, Li G Q, Wang C and Ding W 2012 *Prz Elektrotechnic* **88** 1
[29] Wu Z Q, Ma H, Wang C, Li J H and Zhu J 2019 *Applied Sciences* **9** 744
[30] Li J H, Ma H, Zhang X Q, Luo X Y and Wang C 2021 *Chin. Opt.* **14** 487
[31] Zhang X Q, Wang C, Li J H, Luo X Y, Yu Y J, Xu Y W and Luan X Q 2021 *Opt. Eng.* **60** 084102
[32] Wang C, Luo X Y, Wang C, Jiang H J and Luo C P 2022 *J. Jilin Univ. (Eng. Tech. Ed.)* **52** 3006
[33] Michele N and Donati S 2003 *IEEE T. Instrum. Meas.* **52** 1765
[34] Bes C, Plantier G and Bosch T 2006 *IEEE T. Instrum. Meas.* **55** 1101
[35] Giuliani G, Pietra S B and Donati S 2003 *Meas. Sci. Technol.* **14** 24
[36] Peter J D G, Gregg M G and Steven H M 1988 *Appl. Opt.* **27** 4475
[37] Peter J D G 1990 *J. Mod. Opt.* **37** 1199
[38] Bosch T, Servagent N, Chellali R and Lescure M 1998 *IEEE T. Instrum. Meas.* **47** 13263
[39] Usman Z, Francis B, Bosch T and Aleksandar D R 2010 *IEEE Photonic. Tech. Lett.* **22** 410
[40] Wang X L, Lv L P, Zhu D S, Chen H Q and Huang W C 2022 *Photonics* **9** 430
[41] Xie Z W, Li J, Guo D M, Xia W, Yan H T and Wang M 2024 *Opt. Laser Technol.* **172** 110496
[42] Zhen H, Xu H Z, Wang X H, Tang Y, Shen L H and Li D Y 2024 *Measurement* **229** 114407